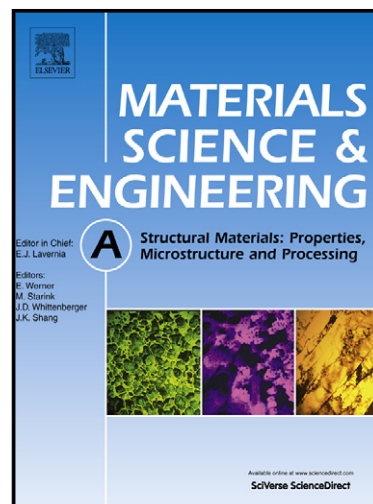# Author's Accepted Manuscript

Static and Dynamic Mechanical Properties of Alumina Reinforced with Sub-Micron Ni Particles

Nathanael L. Barham, Wayne D. Kaplan, Daniel Rittel

MATERIALS SCIENCE & ENGINEERING

A — Structural Materials: Properties, Microstructure and Processing

www.elsevier.com/locate/msea

Cite this article as: Nathanael L. Barham, Wayne D. Kaplan, Daniel Rittel, Static and Dynamic Mechanical Properties of Alumina Reinforced with Sub-Micron Ni Particles, *Materials Science & Engineering A,* http://dx.doi.org/10.1016/j.msea.2013.12.069

Static and Dynamic Mechanical Properties of Alumina Reinforced with Sub-Micron Ni Particles

Nathanael L. Barham[1], Wayne D. Kaplan[2], and Daniel Rittel*[1]

[1]Department of Mechanical Engineering, [2]Department of Materials Science & Engineering

Technion – Israel Institute of Technology, Haifa 32000, Israel

Abstract

This paper reports on the investigation of the static and dynamic properties of an alumina ceramic and nickel alumina nanocomposite and how the ceramic fabrication method affects these properties. In this study, two fabrication methods were used to create the monolithic alumina and the nanocomposites; pressure filtration and slip casting. The static fracture tests followed the ASTM Three Point Bend test while the dynamic fracture tests were conducted using the One Point Impact Test. This study shows that the fabrication method can affect the flexural strength properties of the materials.

Keywords:

Micromechanics

Ceramics

Composites

Failure

Fracture

*Corresponding author:

Email Address: merittel@technion.ac.il
Mailing address:
Materials Mechanics Center, Faculty of Mechanical Engineering, Technion City,
Haifa 32000, Israel
Phone Number: +972-4-829-3261

Introduction

Tensile testing of ceramics has generally been a very difficult process due to complexities with specimen holding and alignment issues. While there are standardized ASTM procedures to obtain the static tensile values, there are no reliable standardized testing methods for the dynamic tensile properties. As a result, there is a significant lack of reliable, published values for the dynamic tensile properties of ceramics. With regards to dynamic flexural strength, there are several testing methods which have been employed (e.g. see Belenky and Rittel, [1] and Delvare et al. [2]). In recent years, the One Point Impact test has been established as a valid method by which reliable dynamic flexural strength values as well as the dynamic fracture toughness values can be determined [1][3]-[8]. This test uses the incident bar of the Split-Hopkinson Pressure Bar [9] in conjunction with the test specimens' inertia to bend the test specimens dynamically. This system was developed based on the work of Böhme and Kalthoff [10], who showed that during the early stages of impact loading in a Three-Point Bend test, the supports do not affect the loading in a specimen. These authors showed that the specimen's inertia during impact loading created flexure which led to the failure of the specimen in bending [10] [11]. The One-Point Impact test is designed around this principle; the test relies on the specimen's inertia to create bending in the specimen. Furthermore, no supports are used in the test not only because they have been shown to be completely irrelevant during the key time period leading up to and ending with the fracture of the specimen, but also because they add a tremendous amount of complexity to the numerical modeling of the test, namely unilateral boundary conditions [1].

Over the past years, much research has been focused on the development of ceramics due to their potential in engineering applications. However, their limited tensile strength is a major disadvantage and is the limiting factor in many ceramic applications [12]. This weakness has fueled research to find a solution whereby the strength of ceramics can be raised.

One solution that has been proven to hold potential is the formation of ceramic matrix composites reinforced with sub-micron particles of a different phase, or "nanocomposites" [13]-[18]. Nanoparticles have been shown to improve the mechanical properties of monolithic ceramics in such areas as hardness, wear resistance, creep resistance, and fracture strength [19]-[21]. The improved mechanical properties are directly related to the interaction between the ceramic matrix grains and the nanoparticles. By controlling and directing the mechanisms that form these microstructural features, one can control and/or achieve specific properties [22] [23].

The location of the nanoparticles within the microstructure is one of the primary sources of many of the improved mechanical properties of nanocomposites [16] [22] [23]. As the ceramic forms, the nanoparticles can be found along the matrix grain boundaries and/or occluded within the matrix grains. The difference between the thermal expansion coefficients of the matrix and nanoparticles generates residual stresses within the nanocomposite upon cooling from the sintering temperature [19]. While several explanations have been offered to explain the mechanism by which the static mechanical strength is improved [19]-[21] [24]

2

[25], the concept of a reduced critical flaw size for crack initiation due to the stress field has become accepted [26] [27].

Unfortunately, conventional mixing of ceramic and nanometer length-scale particles prior to sintering is not only expensive but presents significant health and explosion hazards [22] [28]. As a result, nanocomposites are very expensive to produce and therefore, their use is very limited at this time.

An alternative method to produce metal reinforced nanocomposites is infiltration of the green (bisque-fired) ceramic matrix with aqueous solutions containing metal salts, which are reduced to the metallic state after drying and before sintering to full density. This approach only requires conventional ceramic powder for the matrix material. Metal salts, such as nickel nitrate, are relatively inexpensive and since they are added in a dissolved state, they do not need to be ground into nano-size particles thus eliminating the need for nanoparticles and the hazards and high expenses that accompany them [19] [22] [29]. Furthermore, the desired amount of reinforcing phase can be added via multiple infiltration-drying-reduction stages without the nanoparticles coalescing into micron-size particles [22] [23] [30]. This method also enables different types of metal particles to be deposited during the multiple infiltrations in order to produce a variety of material combinations for specific applications.

In this study, three batches of monolithic alumina and nickel alumina nanocomposites were made using the salt infiltration method. For green body formation, pressure filtration and slip casting were used.

The goal of this work was to measure *both* the static and dynamic tensile mechanical properties of the three different batches of ceramic materials, and assess the extent to which the fabrication process yields any improvement which can be traced back to the microscopic failure mechanisms.

Experimental Methods

Material Processing

In this study, three batches of alumina and nickel reinforced alumina nanocomposites were produced.

Green bodies for the monolithic alumina and nanocomposites were formed using alumina slips containing a mixture of sub-micron alumina powder (Ceralox HPA-0.5), 1 wt.% Mg nitrate, distilled water, and HCl [23]. The HCl was added to disperse agglomerates and to obtain a slurry pH of approximately 4.5 [23]. The Mg nitrate was added to introduce MgO in solution (below the solubility limit) in the alumina to promote the sintering process [31]. The slip was ball-milled for 12 hours using alumina milling balls. From this point, each of the three batches was created slightly differently. The first batch underwent pressure filtration to produce green body disks, which was studied in detail by Gluzer and Kaplan [23]. The second batch underwent slip casting; however, during this process air bubbles formed in the

slip and resulted in voids in the ceramic specimens. The third batch also underwent slip casting to form the green body disks, but the slip was allowed to rest after milling, and was cast into molds at a slower rate to reduce the amount of bubbles. As a result, the samples in the third batch did not contain the voids that were found in the second batch of samples. The green bodies were then air dried for a few days before being heated to 60°C in an air furnace to remove as much water as possible. The green bodies were then (bisque) fired in air at 900°C for two hours in order to promote necking of the particles. At this point, all the samples consisted of pure alumina.

Several disks from each batch were removed and sintered in helium in order to provide control samples. These served as alumina control test specimens. The rest of the unsintered alumina disks were infiltrated with a nickel nitrate solution. The nickel infiltration process involved placing the fired disks in a vacuum desiccator, and then without breaking vacuum, placing the disks in a water-based solution of nickel nitrate. The vacuum removed any air from the open pores in the ceramic disks which helped to ensure penetration of the nickel nitrate solution. The disks were then dried in air for two hours at 60°C and then for five hours at 110°C. In order to form the nickel, the disks were then annealed for 30 minutes at 550°C in an Ar+6%H_2 atmosphere, which converted the nickel nitrate particles to nickel. Samples formed by pressure filtration (first batch) then underwent an additional infiltration process to increase the amount of nickel in the composite. However, the disks for the second and third batch went through the nickel infiltration process only once. After the nickel infiltration process was completed, the disks were sintered in a graphite furnace under flowing helium. Use of a graphite furnace resulted in a low partial pressure of oxygen and ensured reduction of any residual NiO formed due to exposure to the ambient. At the end of the process, there were two types of samples from each batch; pure monolithic alumina, which served as control samples, and nickel-reinforced alumina. Details of the sintering process can be found in Gluzer and Kaplan [23].

In summary, three batches of nanocomposites were produced and tested, and each batch included monolithic alumina as control samples. Batch I was produced using pressure filtration and a double-infiltration process. Batch II was made by slip casting and the samples contained large air bubble voids. Batch III was made using slip casting, but did not contain a significant number of air bubbles. Table 1 lists the amount of nickel in each specimen. The amount of nickel in the material was obtained by weighting the disks before the nickel infiltration process and then after the sintering process, following Aharon et al. [30]. The resulting difference of these two values provided the amount of nickel present in the material.

Nickel Alumina Batch	Wt.% of Nickel
Batch I – Pressure Filtration	~2.2
Batch II – Slip Cast	~1.6
Batch III – Slip Cast	~1.6

Table 1. Percent weight of nickel in each nickel alumina batch.

Static Flexural Strength Procedures

4

The static flexural strength tests followed the procedures outlined by the American Society of Testing and Materials (ASTM) Standard Test Procedure for Flexural Strength of Advanced Ceramics [32], based on three point bending with a test specimen dimension of 3x4x45mm and a loading rate of 0.5mm/min.

Material Property Measurement Procedures

In order to conduct the One Point Impact test, the Young's modulus, Poisson's ratio, and density of the material must be known [1]. We used the Archimedes method to measure the density. The Poisson's ratio was determined by attaching rosette strain gages in the axial and transverse directions on the tensile surfaces of the static test specimens. There was a linear relationship between the load and strains which indicated a consistent Poisson's ratio in the material during static loading. In order to determine the Young's modulus, we first determined the flexural strength of the specimen, based on the recorded peak load. This load was next used in conjunction with the corresponding axial strain to determine the Young's modulus (Hooke's law).

Dynamic Flexural Strength Procedure - One-Point Impact Test

The One Point Impact methodology comprises three steps; the actual test using a Split-Hopkinson Pressure Bar in the One Point Impact loading configuration, extracting the striker bar velocity profile and the time of fracture from test data, and then modeling the actual test using a finite element analysis program to simulate the test. The flexural strength is defined as the tensile stress level experienced by the specimen's outer fiber at the recorded time for the onset of fracture. The test specimens used in this study were identical to the specimens used in the Three Point Bend test. The same manufacturing process and criteria were used for both types of test specimens. For the dynamic test specimens, a thin fracture gage was silk screened on one side of the specimen using a conductive paint in order to determine the exact timing when the specimen began to fracture.

Figure 1 provides a schematic of the one point impact test configuration. The fracture gage was placed on the side of the specimen that would be placed in tension due to the bending of the specimen by the incident bar and the specimen's inertia. On the onset of fracture, the thin fracture gage would also break thereby cutting the electrical circuit. This would instantly register on the oscilloscope and the exact time of fracture would be recorded. A detailed description of the setup of the One Point Impact apparatus can be found in Weisbrod and Rittel [7] and Belenky and Rittel [1] [33] [34]. However, it should be noted that Weisbrod and Rittel [7] measured fracture toughness and, therefore, their test specimens were pre-cracked. Belenky and Rittel [1] [33] [34] measured the dynamic flexural strength and, therefore, their setup was very similar if not identical to the setup up used in this study.
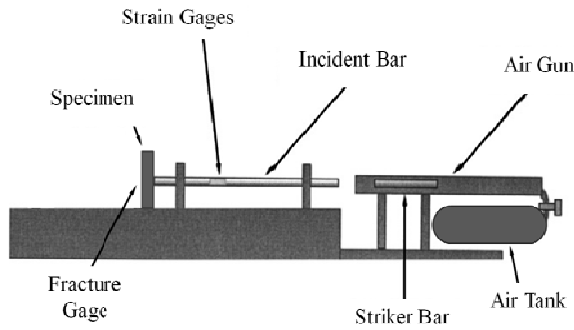
Figure 1. One point impact test configuration of the Split-Hopkinson Pressure Bar.

As Weisbrod and Rittel [7] mentioned, two strain gauges were cemented to opposite sides of the incident bar approximately at the bar's mid-length to eliminate parasitic bending effects in the incident bar. Since the oscilloscope is also connected to the fracture gage, it also recorded when the specimen fractured. Figure 2 shows a typical raw data set from a One Point Impact test. It clearly shows the initial compression wave as well as the next two and a half reflected waves. The Trigger Signal and Fracture Gage signal are also seen synchronized with the initial compression wave.
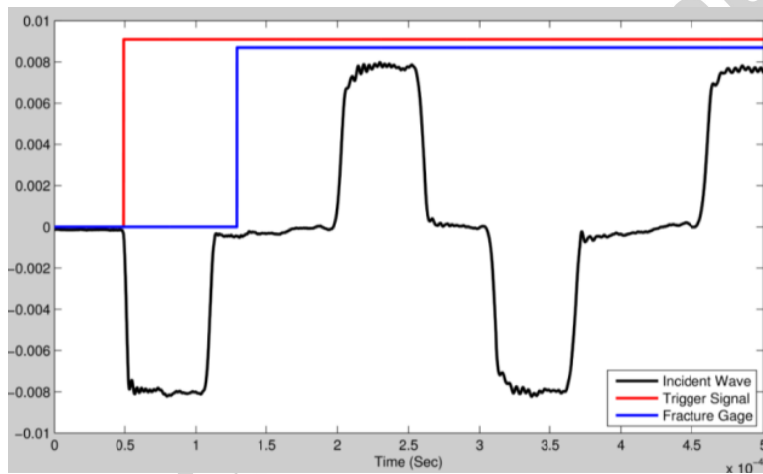
Figure 2. Typical strain measurement measured by the strain gages on the incident bar during a one point impact flexural strength test.

A Cordin 530 high speed camera was also used during the dynamic tests in order to capture the fracture sequence and verify the validity of the tests and to identify the original location of the ceramic fragments for future fractographic analysis. However, due to framing rate limitations (200 kfps), the camera recordings only provided a coarse estimate of the fracture time, and in all cases, we used the actual fracture gage records.

Dynamic Flexural Strength Procedure – Data Acquisition

The next step in determining the dynamic flexural strength of the test specimen involved reducing the oscilloscope reading to obtain the time between the initial compression wave arriving at the strain gages and fracture of the specimen, as well as to obtain the applied

velocity profile to the specimen. This velocity can then be used in the numerical modeling process as a boundary condition, which will be discussed in the next section.

Dynamic Flexural Strength Procedure – Numerical Modeling

The final step in measuring the flexural strength involved modeling the incident bar and ceramic specimen assembly in a Finite Element Analysis program [35] to determine the flexural stress on the tensile side of the ceramic specimen. Due to symmetry, only one quarter of the setup was modeled.

The incident bar's mesh uses the linear C3D8I element which is an 8 node linear hexahedral element enhanced by incompatible modes. Also, it is composed of 16644 elements with an average element side length of approximately 700 µm. The test specimen mesh also uses the linear C3D8I element identical to those used in the incident bar. However, the mesh size of the elements in the test specimen are much smaller; 230 µm with a total number of 11700 elements. In order to check for convergence in the Abaqus model, the mesh size was reduced by half until the difference between the results was less than five percent. The element size that has been specified agreed with this convergence criterion which shows that any further reduction of the mesh size will not produce any considerable change in the flexural strength results. All the analyses were carried out using an explicit integration scheme.

The dynamic loading was applied by means of a velocity boundary condition applied to the end surface of the incident bar that the striker bar contacts. The striker bar's velocity wave profile was added as the velocity boundary condition.

Results and Discussion

Material Properties for Alumina and Nickel Alumina Specimens

Table 2 contains the results of the density, Poisson's ratio, and Young's modulus measurements.

		Density [g/cc]	Percent of Theoretical Density	Poisson's ratio	Young's Modulus [GPa]
Alumina	Batch I (Pressure Filtration)	3.936	99.13[*] (0.695/15 Samples)	0.223 (0.016/6 Samples)	379.9 (NA)
	Batch II (Slip Cast)	3.853	97.06[*] (0.558/19 Samples)	0.236 (0.007/4 Samples)	389.4 (NA)
	Batch III (Slip Cast)	3.926	98.89[*] (0.568/17 Samples)	0.227 (0.007/6 Samples)	398.5 (7.3/6 Samples)

7

|					
Nickel Alumina	Batch I (Pressure Filtration)	3.863	96.15[**] (0.853/18 Samples)	0.219 (NA)	371.6 (NA)
	Batch II (Slip Cast)	3.844	95.95[***] (1.565/18 Samples)	0.249 (0.013/9 Samples)	384.2 (NA)
	Batch III (Slip Cast)	3.919	97.85[***] (1.265/18 Samples)	0.229 (0.008/9 Samples)	383.2 (16.6/9 Samples)

Table 2. Measured values for monolithic alumina and nickel alumina nanocomposites. Standard deviation values and number of samples used to determine the standard deviation values are in parentheses. *The theoretical density of alumina is 3.97g/cc. **The theoretical density of nickel alumina containing ~2.2 wt.% Ni is 4.019g/cc. *** The theoretical density of nickel alumina containing ~1.6 wt.% Ni is 4.006g/cc.

Figure 3 presents the flexural strength for the pressure filtrated material (Batch I) and shows the average static flexural strength of the nickel alumina specimens to be approximately 85 MPa weaker than the static flexural strength of the alumina (490 MPa and 575 MPa respectively), and the average dynamic flexural strength of the nickel alumina value to be approximately 115 MPa stronger than the average dynamic flexural strength of the alumina (960 MPa and 875 MPa respectively). Figure 3 shows the alumina and nickel alumina both possess a strain rate sensitivity in that the materials' flexural strength significantly changed between the static and dynamic strain rates. Furthermore, while they both have significant dynamic flexural strength, the nickel particles seem to give the nickel alumina slightly more dynamic flexural strength compared to the alumina specimens. However, it should be noted that only two valid data points were obtained for the dynamically fractured alumina tests, and therefore it is difficult to extract a lot of information from this data. Regardless, both the alumina and the nickel alumina possess a significant dynamic flexural strength.
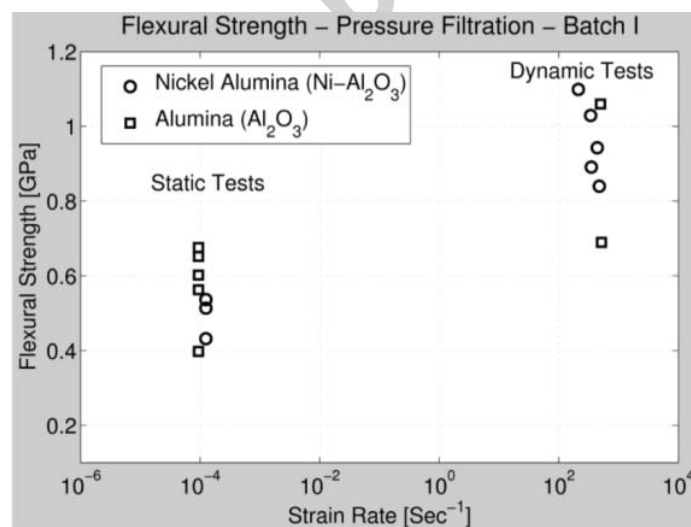
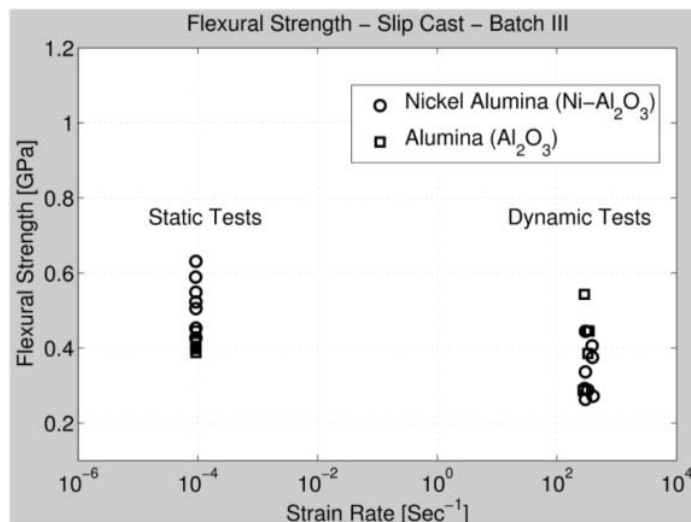**Figure 3. Static and dynamic flexural strength data for Batch I – Pressure Filtration.**

8

Batch II was made using slip casting and during the formation of the material, air bubbles were formed in the slip which resulted in voids or air pockets once the sintering process was completed. While the fractographic analysis will be discussed later, it should be noted here that the fractographic analysis showed that for all the static tests, the fracture origins were located at an air bubble void. In the dynamic tests, approximately half the test specimens were directly affected by the air bubble voids. While flaws are inherent in any ceramic material, the air bubbles (voids) were preventable and significantly larger than the normal inherent flaws. Therefore, these air bubbles are an abnormal type of flaw in the material. Furthermore, since they were the source of the fracture origins in the vast majority of the tests, these tests were questionable. Most of the flexural strength values therefore do not reflect the "actual" material properties since it is not currently possible to model the air bubbles in the dynamic tests. Figure 4 shows that there were no differences between the static and dynamic flexural strengths for either the alumina or nickel alumina. This figure indicates that these specimens likely reflect how the size and location of the air bubble voids affected the flexural strength.
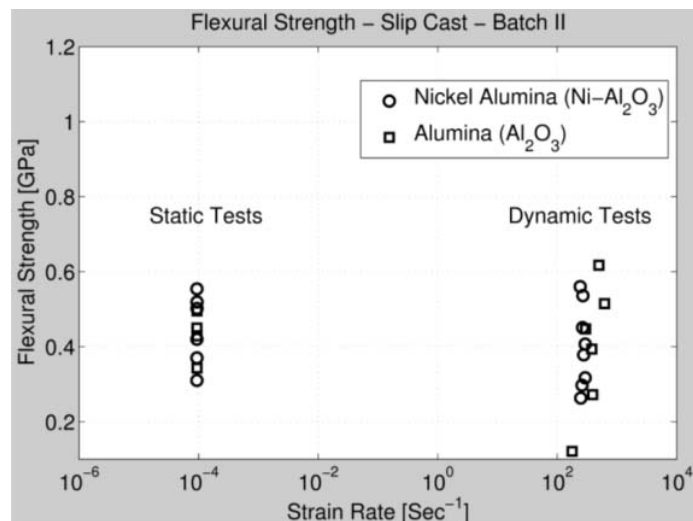
Figure 4. Static and dynamic flexural strength data for Batch II - Slip Casted.

Batch III was also made using slip casting. However, more care was taken during the manufacturing process to prevent the formation of air bubbles in the slip. As a result, Batch III did not contain a significant amount of air bubble voids. The flexural strength values for Batch III are presented in Figure 5 which shows no form of strain rate sensitivity in the alumina while possibly a little negative strain rate sensitivity in the nickel alumina. However, this apparent negative strain rate sensitivity could simply be a result of a scarcity of nickel particles, which will be discussed in the next section. It is evident from this figure though, that the nickel alumina specimens had a greater static flexural strength than the alumina specimens. The average static flexural strength for the alumina and nickel alumina is 410 MPa and 525 MPa respectively. While the nickel particles increased the flexural strength in the static regime, the nickel particles did not increase the strength in the dynamic regime. In fact, the average dynamic flexural strength of the nickel alumina dropped to 330 MPa while

the average dynamic flexural strength of the alumina rose to 420 MPa; 90 MPa higher than the nickel alumina.

**Figure 5. Static and dynamic flexural strength data for Batch III - Slip Casted.**

Fractographic Results for the Pressure Filtrated Material (Batch I)

The fractographic analysis showed that all the statically fractured specimens had flaws at their facture origins. These flaws included surface and internal cracks, cavities, voids, porous regions, and agglomerates. Characterizing and measuring the flaws showed the general and somewhat expected trend that as the flaws increase in size and proximity to the tensile edge, the strength of the specimen decreases. Due to extreme temperatures that ceramics must go through during manufacturing and the subsequent cooling, small cracks and flaws are expected due to residual stresses created as the ceramic contracts during the cooling phase. However, larger voids and flaws can negatively affect the test results to the point where the test is measuring the strength of the flaw and not the material properties. As a result, test specimens with abnormally large flaws were removed. The fractographic analysis showed that while the valid specimens were not flaw-free, the flaws were relatively small and the flaws and their locations were similar with the other statically and dynamically fractured specimens.

Scanning electron microscopy (SEM) micrographs from the strongest statically fractured pressure filtrated alumina and nickel alumina specimens are presented in Figures 6-8, and are a typical representation of this group.
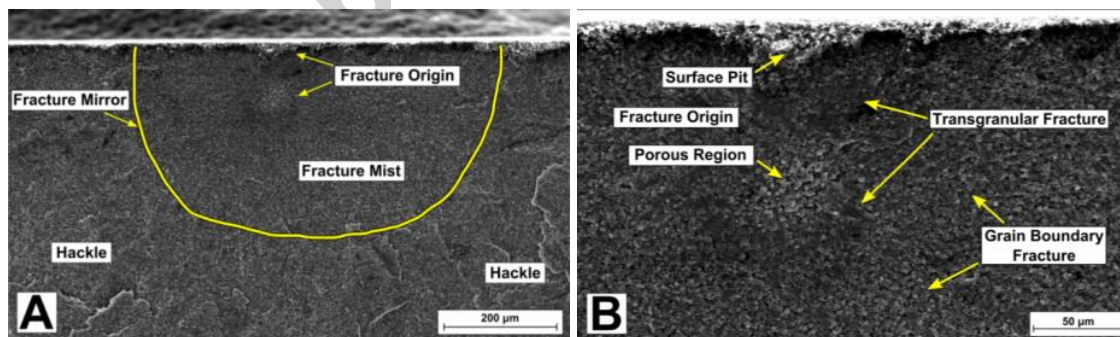
The strongest statically fractured alumina specimen is shown in Figure 6A and B. The fracture origin was clearly identified from the clear fracture mirror surrounded by a hackle. It is located along the tensile edge of the specimen and a closer inspection of the fracture origin shows a cavity at this location. The cavity does not appear to have been created during machining and therefore, it was simply a material flaw that formed during manufacturing of

the ceramic. There is a significant amount of transgranular fracture to the left of the cavity which then transitions to grain boundary fracture (or intergranular fracture).
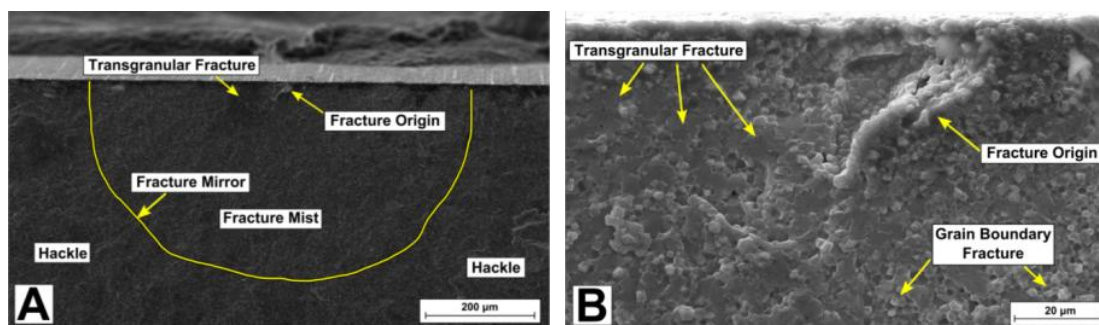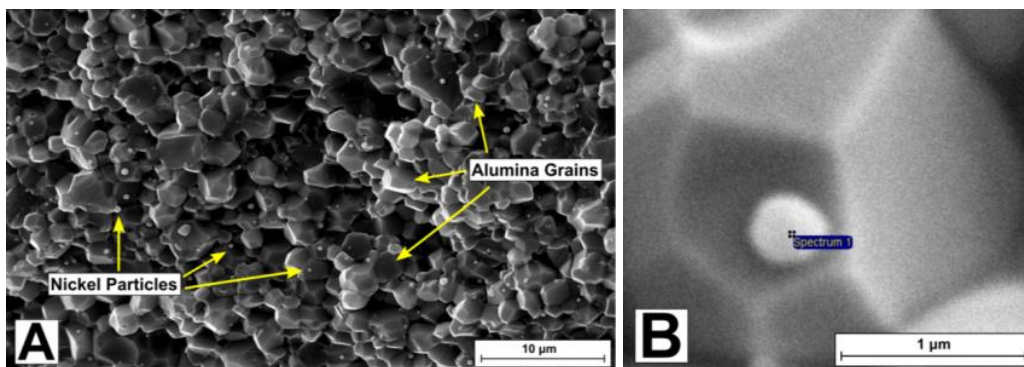

Figure 6. Secondary electron SEM micrographs of the fracture surface of a statically fractured pressure filtrated alumina specimen (flexural strength 675 MPa) showing the fracture mirror (A) and grain boundary and transgranular fracture around the fracture origin (B).

Figures 7-8 show the fracture origin of the strongest statically fractured nickel alumina specimen which had a flexural strength of 540 MPa. The fracture origin is identified from the clearly delineated hackle and fracture mirror, Figure 7A. Figure 7B shows the fracture origin to be caused by a surface pit and an internal porous region approximately 75µm from the tensile edge. Transgranular fracture surrounds most of the porous area and almost half of the area between the porous area and the surface pit. The amount of transgranular fracture is far less than was present in the statically fractured alumina specimen, although there was a significant amount of transgranular fracture across the fracture surface. Finally, there was also a large distribution of visible nickel particles in this specimen as can be seen in Figure 8A, and which were confirmed to be nickel from energy dispersive spectroscopy (EDS). The nickel particles are distributed along grain boundaries of the alumina.
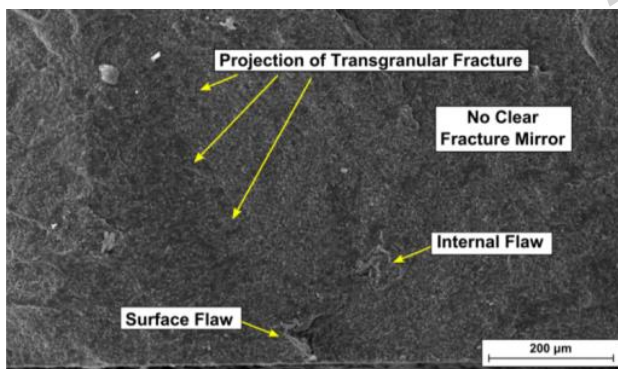

Figure 7. Secondary electron SEM micrographs of the fracture surface of a statically fractured pressure filtrated nickel alumina specimen (flexural strength 535 MPa) showing the fracture mirror (A) and the fracture origins with the transgranular and grain boundary fracture (B).

11

Figure 8. (A) Secondary electron SEM micrograph of the fracture surface of a statically fractured pressure filtrated nickel alumina specimen (flexural strength 535 MPa) showing an abundance of nickel particles amongst the alumina grains and (B) a higher magnification backscattered micrograph of a nickel particle on an alumina grain.

A SEM micrograph of the strongest dynamically fractured alumina specimen is shown in Figure 9. The fracture mirror is not as clearly delineated in this specimen; however, the fracture origin was identified as originating at a surface cavity and an internal cavity caused during manufacturing of the material. There is a significant amount of transgranular fracture around the fracture origin with one "finger" or projection of transgranular fracture stretching approximately 600μm into the material.
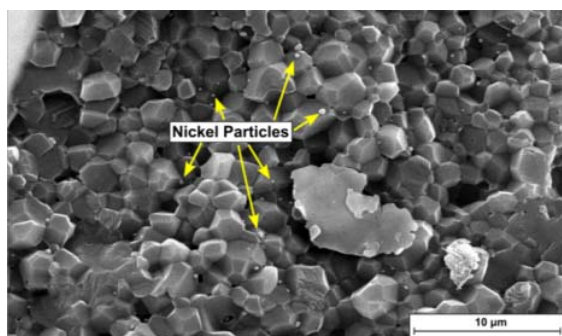

Figures 9. Secondary electron SEM micrograph of a dynamically fractured pressure filtrated alumina specimen; flexural strength 1060 MPa.

Figure 10A shows the fracture origin for the strongest dynamically fractured nickel alumina specimen with a flexural strength of 1100 MPa. The fracture mirror is very vague in this specimen. The exact cause of the fracture is unknown partly due to the two large contaminate bodies (originating from the SEM specimen preparation process) that cover the location (Figures 10B). Transgranular fracture is the primary form of fracture within a 50-70 µm radius of the fracture origin; however, compared to the dynamically fractured alumina specimen, there is considerably less transgranular fracture around the fracture origin. On the other hand, there was a significant amount of transgranular fracture throughout the rest of the fracture surface. Also, here again, there was a significant distribution of visible nickel particles throughout the material (Figure 11).
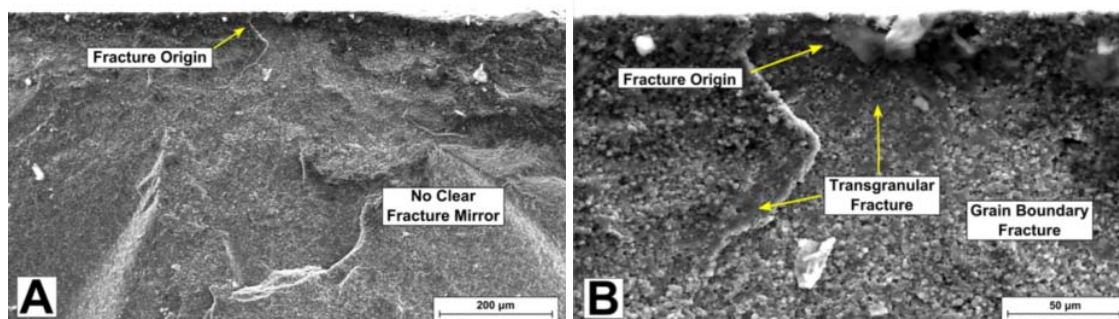
Figure 10. Secondary electron SEM micrographs of the fracture surface from a dynamically fractured pressure filtrated nickel alumina specimen showing the lack of a clear fracture mirror (A) (flexural strength 1100 MPa) and the fracture origin and transgranular and grain boundary fracture (B).

Figure 11. A higher magnification secondary electron SEM micrograph of the fracture surface of the dynamically fractured pressure filtrated nickel alumina specimen (flexural strength 1100 MPa) showing nickel particles distributed amongst the alumina grains.

The fracture surfaces of the slip casted specimens of Batch III were examined and characterized in a manner similar to the pressure filtrated specimens of Batch I. The results were very similar to the pressure filtrated material in almost every aspect.
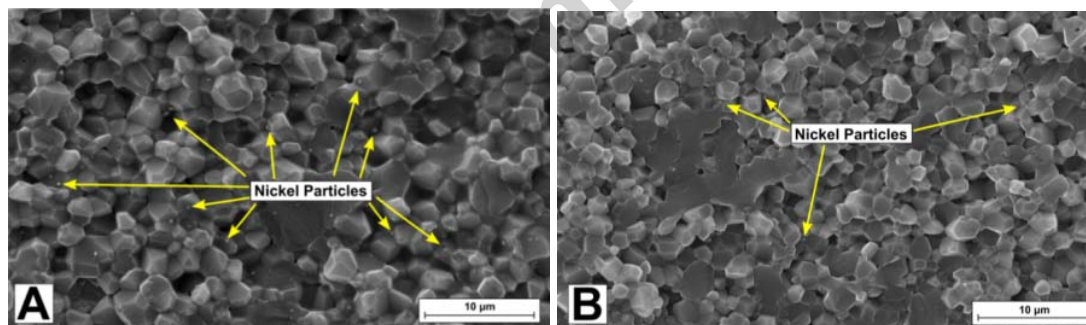
First, the fracture surfaces of both the pressure filtrated and slip casted material show that in general, as the flaws grew larger and closer to the tensile edge, the specimens grew weaker.

Second, transgranular fracture and grain boundary fracture occurred in both the pressure filtrated and slip casted material in similar proportions and dispersion; in general, there was approximately equal amounts of transgranular fracture and grain boundary fracture on the fracture surfaces. The alumina specimens had considerably more transgranular fracture around the fracture origin than the nickel alumina. However, the nickel alumina specimens had more transgranular fracture throughout the fracture surfaces than the alumina.

Third, in both the pressure filtrated and slip casted materials, the stronger specimens, regardless of the whether they were loaded statically or dynamically, possessed the more

vague fracture mirrors. The size and clarity of the fracture mirror is related to the strength of the specimen; the larger the fracture mirror, the weaker the specimen [36]. This relation between the strength of the specimen and the roughness of the mirror-mist-hackle sequence is related to the crack velocity. Consequently, a small or non-existent mirror zone indicates that the crack propagated through the material with a high velocity in conjunction to a significant release of accumulated strain energy. In turn, the larger amount of accumulated strain energy is a direct indication of the strength of the material. As a result, the smaller fracture mirror corresponds to a higher crack velocity, a higher accumulation of strain energy, and therefore, a stronger material. Both the pressure filtrated and slip cast materials agreed with this principle.

The only difference in the fractographic analysis of the pressure filtrated and slip casted fracture surfaces involved the amount of visible nickel particles in the nickel alumina materials. There was a consistent abundance of visible nickel particles throughout the fracture surfaces of the pressure filtrated material as Figures 8A and 11 have shown. However, the amount of visible nickel varied considerably throughout the facture surfaces of the slip casted material. The visible nickel was very abundant in the stronger slip casted specimens (~500-600 MPa) and noticeably lacking in the weaker specimens (~200-400 MPa). Figures 12A (secondary electrons) and 13A (backscattered electrons) show the surface from a statically fractured nickel alumina specimen which had a high flexural strength. Figures 12B (secondary electrons) and 13B (backscattered electrons) show the surface from a dynamically fractured specimen which had a low flexural strength.


Figure 12. Secondary electron SEM micrographs of the fracture surfaces of (A) a statically fractured nickel alumina specimen (flexural strength 630 MPa) and (B) a dynamically fractured nickel alumina specimen (Flexural strength 445 MPa) showing the difference between the amount of nickel particles between the statically and dynamically fractured specimens.

14
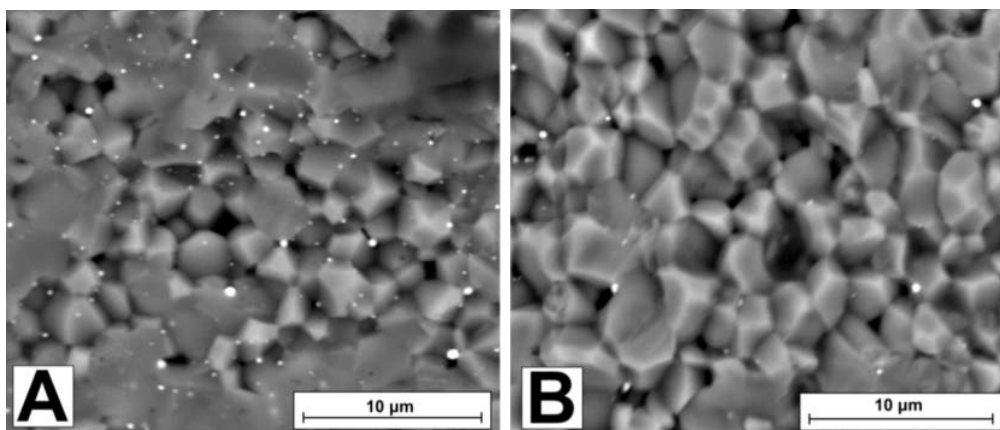
Figure 13.   The fracture surface of a statically fractured nickel alumina specimen (A) and a dynamically fractured nickel alumina specimen (B) showing the amount of nickel in the specimens using backscattered SEM.   The alumina particles are the large gray grains while the nickel particles are the smaller white spots.

This large variation in local density of the visible nickel particles was seen throughout the slip-casted material and seems to have significantly impacted the strength of the material. An inhomogeneous distribution of particles within a nanocomposite is known to significantly reduce the mechanical properties of a material, and can often be a cause of fracture [25]. Comparing all the statically fractured pressure filtrated and slip casted nickel alumina, Figure 14, and all the dynamically fractured pressure filtrated and slip casted nickel alumina, Figure 15, supports this theory. The statically fractured slip casted nickel alumina specimens had a similar abundant distribution of visible nickel particles as the statically fractured pressure filtrated nickel alumina specimens and their flexural strengths were very similar, Figure 14. However, the dynamically fractured slip casted nickel alumina specimens lacked the uniform abundance of visible nickel particles which the dynamically fractured pressure filtrated nickel alumina specimens possessed. As a result, the slip casted specimens possessed drastically lower dynamic flexural strength than the pressure filtrated specimens, Figure 15. Therefore, when comparing the quality of the nanocomposites, the pressured filtration fabrication method produced a superior material than the slip casting method due to the more uniform distribution of the visible nickel particles.
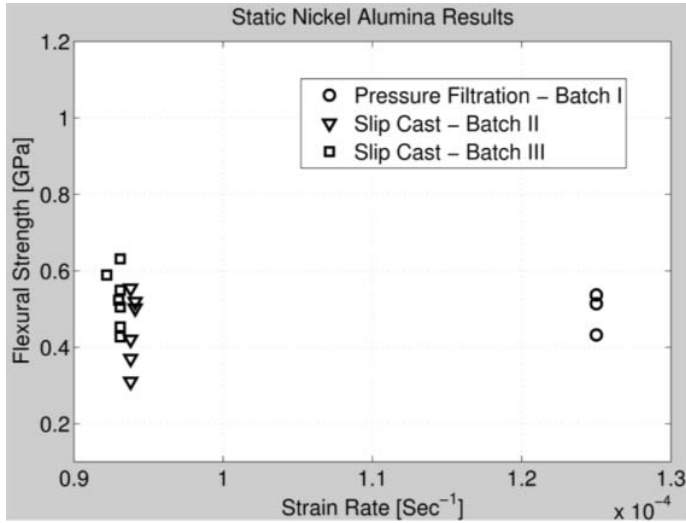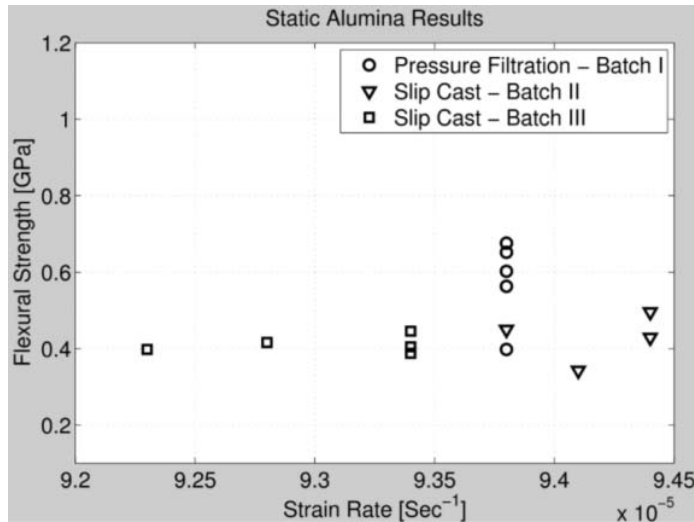
15

Figure 14. Static flexural strength values of all the nickel alumina samples in Batches I (Pressure Filtration), II (Slip-Casted), & III (Slip-Casted).
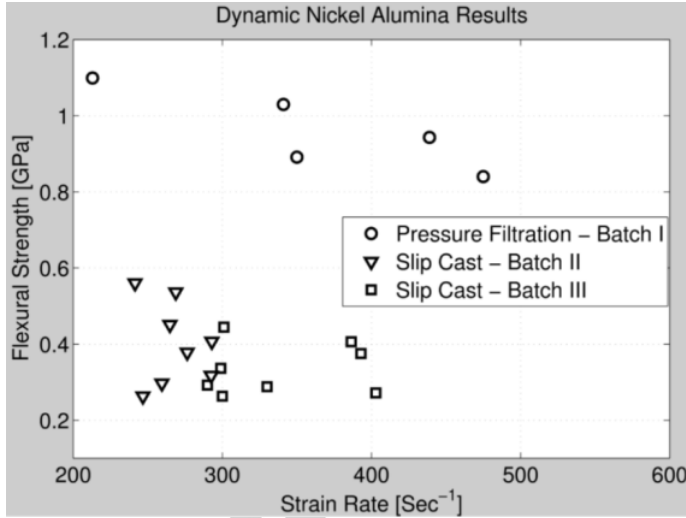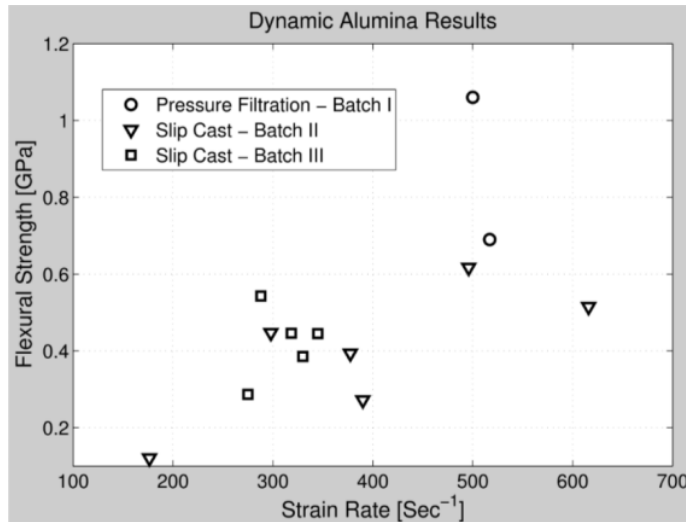

Figure 15. Dynamic flexural strength values of all nickel alumina samples in Batches I (Pressure Filtration), II (Slip-Casted), & III (Slip-Casted).

The uniformity of the visible nickel distribution is not the only cause for the difference in flexural strength results between the slip cast and pressure filtrated materials. If it were, the static and dynamic flexural strength values for the slip cast and pressure filtrated alumina would be very similar since the uniformity of the distribution of the nickel particles is not relevant. However, when comparing the static flexural strength of the pressure filtrated and slip cast materials (Figure 16) and the dynamic flexural strength of the pressure filtrated and slip cast materials (Figure 17), the pressure filtrated material clearly has higher flexural strength values. When comparing the alumina results, one is simply comparing the pressure filtrated and slip cast fabrication methods. Figures 16-17 clearly show that the pressure filtration fabrication method produced superior material with regards to the flexural strength when compared to the material produced by the slip cast fabrication method.

16

Figure 16. **Static flexural strength values of all the alumina samples in Batches I (Pressure Filtration), II (Slip-Casted), and III (Slip-Casted).**

Figure 17. **Dynamic flexural strength values of all the alumina samples in Batches I (Pressure Filtration), II (Slip-Casted), and III (Slip-Casted).**

Finally, as a general observation, one should first note that the literature cited in the introductory section reports a general trend for an increased dynamic initiation toughness and strength in quasi-brittle materials, be it polymers, bulk metallic glasses or low ductility metals. In this work, three different batches have been tested and for each batch, a specific dynamic to static flexural strength relationship was observed which was not monotonous. Namely, this work does not reveal a uniform increase in the dynamic flexural strength of the batches, irrespective of their fabrication route. It can thus be concluded that the present observation lends additional reliability to the adopted test methodology, which is capable of discriminating between different fabrication routes when all the experimental parameters were kept identical for all the tested specimens in this study.

17

Conclusions

This study focused on analysis of the static and dynamic flexural strengths of polycrystalline alumina compared to alumina reinforced with sub-micron particles of nickel. Two fabrication methods were used to create the green bodies prior to introduction of nickel into the various specimens; pressure filtration and slip casting. The static and dynamic flexural strength of the resulting alumina and nickel alumina composites were measured, and the fracture surfaces were examined to evaluate the failure micromechanisms. The conclusions of this research project are as follows:

1. The pressure filtrated alumina had an average static and dynamic flexural strength of 575 MPa and 875 MPa respectively while the pressure filtrated nickel alumina composite had an average static and dynamic flexural strength of 490 MPa and 960 MPa respectively. The pressure filtrated alumina and nickel alumina specimens possessed a strain rate sensitivity.
2. The slip cast alumina had an average static and dynamic flexural strength of 410 MPa and 420 MPa, respectively, while the slip cast nickel alumina composite had an average static and dynamic flexural strength of 525 MPa and 330 MPa, respectively. The slip cast alumina and nickel alumina composite were not sensitive to strain rate.
3. Approximately equal amounts of transgranular and grain boundary fracture occurred in both the pressure filtrated and slip cast alumina and nickel alumina specimens.
4. The fabrication method affects the uniformity of the visible nickel nanoparticle distribution within the microstructure, with the pressure filtration method providing a more uniform distribution than the slip cast method.
5. The fabrication method used to make the green bodies affects the flexural strength of the resulting material, with the pressure filtration method producing a material with a higher flexural strength than the slip cast method, particularly at higher strain rates.
6. The reliability of the One Point Impact test methodology increased due to its ability to reflect both high and low flexural strength values.

Acknowledgements

References

[1] A. Belenky, D. Rittel, Exp. Mech. 51 (2011) 1325-1334.

[2] F. Delvare, J.L. Hanus, P. Bailly, Int. J. Impact Eng. Vol. 37 Issue 12 (2010) 1170-1179.

[3] D. Rittel, H. Maigre, H.D. Bui, Scr. Metallurgica et Mater. 26 (1992) 1593-1598.

[4] D. Rittel, G. Weisbrod, Inter. J. Fract. 112 (2001) 87-98.

[5] D. Rittel, N. Frage, M.P. Dariel, Inter. J. Solids Struct. 42 (2005) 697-715.

[6] A. Belenky, I. Bar-On, D. Rittel, J. Mech. Phys. Solids 58 (2010) 484-501.

[7] G. Weisbrod, D. Rittel, Inter. J. Fract. 104 (2000) 89-103.

[8] S. Hayun, D. Rittel, N. Frage, M.P. Dariel, Mater. Sci. Eng. A 487 (2008) 405-409.

[9] H. Kolsky, Proceedings of the Phys. Soc. Section B 62 (1949) 676-700.

[10] W. Böhme, J.F. Kalthoff, Inter. J. Fract. 20 (1982) R139-R143.

[11] J.H. Giovanola, In: J.G. Underwood et al. (Eds.), Fracture Mechanics: Vol. 17 ASTM-STP 905. Philadelphia, PA., Am. Soc. Test. Mater. 1986.

[12] M. Nawa, T. Sekino, K. Niihara, J. Mater. Sci. 29 (1994) 3185-3192.

[13] K. Niihara, K. Suganuma, A. Nakahira, K. Izaki, J. Mater. Sci. Lett. 9 (1990) 598-599.

[14] J. Zhao, L.C. Stearns, M.P. Harmer, H.M. Chan, G.A. Miller, R.F. Cook, J. Am. Ceram. Soc. 76 (1993) 503-510.

[15] I. Levin, W.D. Kaplan, D.G. Brandon, T. Wieder, Acta Metallurgica et Mater. 42 (1994) 1147-1154.

[16] I. Levin, W.D. Kaplan, D.G. Brandon, A.A. Layyous, J. Am. Ceram. Soc. 78 (1995) 254-256.

[17] T. Sekino, T. Nakajima, K. Niihara, Mater. Lett. 29 (1996) 165-169.

[18] T. Sekino, T. Nakajima, S. Ueda, K. Niihara, J. Am. Ceram. Soc. 80 (1997) 1139-1148.

[19] M. Lieberthal, W.D. Kaplan, Mater. Sci. Eng. A 302 (2001) 83-91.

[20] T. Ohji, T. Hirano, A. Nakahira, K. Niihara, J. Am. Ceram. Soc. 79 (1996) 33-45.

[21] T. Ohji, Y.K. Jeong, Y.H. Choa, K. Niihara, J. Am. Ceram. Soc. 81 (1998) 1453-1460.

[22] W.D. Kaplan, A. Avishai, in: I.M. Low (Ed.), Ceramic Matrix Composites: Microstructure, Properties, and Applications. Woodhead Publishing, Sawston, Cambridge, 2006, pp. 285-308.

[23] G. Gluzer, W.D. Kaplan, J. Eur. Ceram. Soc. 33 (2013) 3101-3113.

[24] K. Niihara, J. Ceram. Soc. Jpn. 99 (1991) 974-982.

[25] S.T. Oh, M. Sando, K. Niihara, J. Mater. Sci. 36 (2001) 1817-1821.

[26] X. Sun, J.G. Li, S. Guo, Z. Xiu, K. Duan, X.Z. Hu, J. Am. Ceram. Soc. 88 (2005) 1536-1543.

[27] L.P. Ferroni, G. Pezzotti, J. Am. Ceram. Soc. 85 (2002) 2033-2038.

[28] A. Seaton, L. Tran, R. Aitken, K. Donaldson, J. R. Soc. Interface 7 (2010) S119-S129.

[29] M. Sternitzke, J. Eur. Ceram. Soc. 17 (1997) 1061-1082.

[30] O. Aharon, S. Bar-Ziv, D. Gorni, T. Cohen-Hyams, W.D. Kaplan, Scr. Mater., 50 [9] (2004) 1209-1213.

[31] L. Miller, A. Avishai, W.D. Kaplan, J. Am. Ceram. Soc., 89 [1] (2006) 350-353.

[32] ASTM-C1161, Am. Stand. Test. Mater. (2008).

[33] A. Belenky, D. Rittel, Mech. Mater. 48 (2012) 43-55.

[34] A. Belenky, D. Rittel, Mech. Mater. 54 (2012) 91-99.

[35] Abaqus/CAE6.9-PF2, Dassault Systemes Simulia Corporation, Providence, RI, USA, 2009.

[36] G.D. Quinn, Fractography of Ceramics and Glasses, Special Publication 960-17 ed., National Institute of Standards and Technology, Washington D. C. 2007.

Nickel Alumina Batch	% Wt. of Nickel
Batch I – Pressure Filtration	~2.2
Batch II – Slip Cast	~1.6
Batch III – Slip Cast	~1.6

		Density [g/cc]	Percent of Theoretical Density	Poisson's ratio	Young's Modulus [GPa]
Alumina	Batch I (Pressure Filtration)	3.936	99.13[*] (0.695/15 Samples)	0.223 (0.016/6 Samples)	379.9 (NA)
	Batch II (Slip Cast)	3.853	97.06[*] (0.558/19 Samples)	0.236 (0.007/4 Samples)	389.4 (NA)
	Batch III (Slip Cast)	3.926	98.89[*] (0.568/17 Samples)	0.227 (0.007/6 Samples)	398.5 (7.3/6 Samples)
Nickel Alumina	Batch I (Pressure Filtration)	3.863	96.15[**] (0.853/18 Samples)	0.219 (NA)	371.6 (NA)
	Batch II (Slip Cast)	3.844	95.95[***] (1.565/18 Samples)	0.249 (0.013/9 Samples)	384.2 (NA)
	Batch III (Slip Cast)	3.919	97.85[***] (1.265/18 Samples)	0.229 (0.008/9 Samples)	383.2 (16.6/9 Samples)

Article: **Static and Dynamic Mechanical Properties of Alumina Reinforced with Sub-Micron Ni Particles**

Nathanael L. Barham, Wayne D. Kaplan, and Daniel Rittel*

*Corresponding author:

Email Address: merittel@technion.ac.il,

Mailing address: Materials Mechanics Center, Faculty of Mechanical Engineering, Technion City, Haifa 32000, Israel

Phone Number: +972-4-829-3261

Table 1. Percent weight of nickel in each nickel alumina batch.

Figure 1. One point impact test configuration of the Split-Hopkinson Pressure Bar.

Figure 2. Typical strain measurement measured by the strain gages on the incident bar during a one point impact flexural strength test.

Table 2. Measured values for monolithic alumina and nickel alumina nanocomposites. Standard deviation values and number of samples used to determine the standard deviation values are in parentheses. *The theoretical density of alumina is 3.97g/cc. **The theoretical density of nickel alumina containing ~2.2 wt.% Ni is 4.019g/cc. *** The theoretical density of nickel alumina containing ~1.6 wt.% Ni is 4.006g/cc.

Figure 3. Static and dynamic flexural strength data for Batch I – Pressure Filtration.

Figure 4. Static and dynamic flexural strength data for Batch II - Slip Casted.

Figure 5. Static and dynamic flexural strength data for Batch III - Slip Casted.

Figure 6. Secondary electron SEM micrographs of the fracture surface of a statically fractured pressure filtrated alumina specimen (flexural strength 675 MPa) showing the fracture mirror (A) and grain boundary and transgranular fracture around the fracture origin (B).

Figure 7. Secondary electron SEM micrographs of the fracture surface of a statically fractured pressure filtrated nickel alumina specimen (flexural strength 535 MPa) showing the fracture mirror (A) and the fracture origins with the transgranular and grain boundary fracture (B).

Figure 8. (A) Secondary electron SEM micrograph of the fracture surface of a statically fractured pressure filtrated nickel alumina specimen (flexural strength 535 MPa) showing an abundance of nickel particles amongst the alumina grains and (B) a higher magnification backscattered micrograph of a nickel particle on an alumina grain.

Figures 9. Secondary electron SEM micrograph of a dynamically fractured pressure filtrated alumina specimen; flexural strength 1060 MPa.

Figure 10. Secondary electron SEM micrographs of the fracture surface from a dynamically fractured pressure filtrated nickel alumina specimen showing the lack of a clear fracture mirror (A) (flexural strength 1100 MPa) and the fracture origin and transgranular and grain boundary fracture (B).

Figure 11. A higher magnification secondary electron SEM micrograph of the fracture surface of the dynamically fractured pressure filtrated nickel alumina specimen (flexural strength 1100 MPa) showing nickel particles distributed amongst the alumina grains.

Figure 12. Secondary electron SEM micrographs of the fracture surfaces of (A) a statically fractured nickel alumina specimen (flexural strength 630 MPa) and (B) a dynamically fractured nickel alumina specimen (Flexural strength 445 MPa) showing the difference between the amount of nickel particles between the statically and dynamically fractured specimens.

Figure 13. The fracture surface of a statically fractured nickel alumina specimen (A) and a dynamically fractured nickel alumina specimen (B) showing the amount of nickel in the specimens using backscattered SEM. The alumina particles are the large gray grains while the nickel particles are the smaller white spots.

Figure 14. Static flexural strength values of all the nickel alumina samples in Batches I (Pressure Filtration), II (Slip-Casted), & III (Slip-Casted).

Figure 15. Dynamic flexural strength values of all nickel alumina samples in Batches I (Pressure Filtration), II (Slip-Casted), & III (Slip-Casted).

Figure 16. Static flexural strength values of all the alumina samples in Batches I (Pressure Filtration), II (Slip-Casted), and III (Slip-Casted).

Figure 17. Dynamic flexural strength values of all the alumina samples in Batches I (Pressure Filtration), II (Slip-Casted), and III (Slip-Casted).